A Comprehensive Evaluation of Contact Recombination and Contact Resistivity Losses in Industrial Silicon Solar Cells

Mengjie Li [ID], Nafis Iqbal, Zhihao Yang [ID], Xuli Lin, Nicole Karam Pannaci [ID], Christian Avalos, Thomas Shaw, Titel Jurca, and Kristopher Davis [ID]

Abstract—**Reliable characterization techniques to accurately quantify the metallization-induced recombination losses as well as contact resistivity losses of screen-printed cells are crucial for successful optimization of the contact grid design. Previously, the dark saturation current density at the contact (J_{0c}) is often assumed to be constant for different finger width. Similarly, impact of finger width on contact resistivity (ρ_c) is rarely reported. Therefore, we performed a comprehensive evaluation of J_{0c} and ρ_c as a function of finger width, spacing as well as firing temperature. We found out that J_{0c} increases from $\approx$2000 to $\approx$8100 fA/cm^2, when the finger width increases from 60 to 400 μm; and ρ_c decrease from 7.2 to 2.2 m$\Omega \cdot$ cm^2 when using a *wide*-TLM rather than a *narrow*-TLM structure, for samples fired at 840 °C. Based on our cross-sectional and top-down scanning electron microscopy images, we believe that the physical root cause can be explained by the difference in the microstructure formed at the metal–silicon interface during the firing process for the screen-printed contacts.**

Index Terms—**Contact recombination, *c*-Si, photoluminescence (PL), photovoltaic (PV) cells, screen printing.**

I. INTRODUCTION

SCREEN printing is widely used in the photovoltaic (PV) industry due to its robust, simple, and highly automated process, as well as rapid developments in the metallization pastes.

Mengjie Li and Nafis Iqbal are with the Department of Materials Science and Engineering, University of Central Florida, Orlando, FL 32816 USA (e-mail: mengjie.li@ucf.edu; nafisiqbal@Knights.ucf.edu).

Zhihao Yang is with the School of Materials Science and Energy Engineering, Foshan University, Guangdong 528000, China and is also with Guangdong Nanhai ETEB Technology Company, Ltd., Guangdong 528251, China (e-mail: pvtech@qq.com).

Xuli Lin is with the Guangdong Nanhai ETEB Technology Company, Ltd., Guangdong 528251, China (e-mail: xuli.lin@eteb.com.cn).

Nicole Karam Pannaci and Christian Avalos are with the Department of Electrical and Computer Engineering, University of Central Florida, Orlando, FL 32816 USA (e-mail: karana@knights.ucf.edu; cavalos@Knights.ucf.edu).

Thomas Shaw and Titel Jurca are with the Department of Chemistry, University of Central Florida, Orlando, FL 32816 USA and is also with Renewable Energy and Chemical Transformations Cluster, University of Central Florida, Orlando, FL 32816 USA (e-mail: TShaw@knights.ucf.edu; Titel.Jurca@ucf.edu).

Kristopher Davis is with the Department of Materials Science and Engineering, University of Central Florida, Orlando, FL 32816 USA and is also with Resilient, Intelligent and Sustainable Energy Systems (RISES) Cluster, University of Central Florida, OrlandoFL 32816 USA (e-mail: kristopher.davis@ucf.edu).

Color versions of one or more of the figures in this article are available online at https://ieeexplore.ieee.org.

Digital Object Identifier 10.1109/JPHOTOV.2020.3003792

Metallization pastes using Ag are the most process-critical and most expensive nonsilicon material used in the solar cell fabrication process. Optimizing the contact grid design, reducing the paste consumption while maintaining and improving the performance of screen-printed solar cells is critical. For screen-printed contacts, the electrical contact to Si is formed during a subsequent firing step, where the glass frit in the paste melt and chemically etch through the dielectric passivation layer and react with the doped Si. The contact formation during the firing process is a critical step, as the metal–silicon interfaces form a highly recombination active surface for minority charge carriers [1]. The contact recombination losses need to be constrained. Meanwhile, a high-quality ohmic contact has to be formed to make sure that contact resistivity loss is low. In order to optimize the metallization process, reliable characterization techniques are needed to accurately quantify the metallization-induced recombination losses as well as contact resistivity losses.

Several approaches attempt to extract saturation current density at the contact (J_{0c}) have been reported over the years [1]–[6]. Evaluations on the metallization-induced recombination losses by numerical device simulations were reported in [3], [6], and [7], where the morphologies of the metal–Si interface and J_{0c} were commonly used as fitting parameters to explain the experimentally observed open-circuit voltage (V_{oc}) losses of finished solar cells. Thus, it is challenging to get an accurate quantitative understanding with the numerical simulations. Another common approach to obtain J_{0c} is by fabricating minicells with varying metal fraction by either changing the finger width or changing the finger spacing [1], [2], [4]. Then, by suns-V_{oc} measurement and fitting the curves with a one-diode model, total J_0 can be calculated, and subsequently, J_{0c} can be calculated based on the known metal fraction. However, as pointed out by Herrmann *et al.*[8], this area-weighted approach leads to an underestimation of J_{0c}, since the nonuniformities of the excess carrier density in the sample were not considered in the calculation. Additionally, since the metal fraction has to be used as a fitting parameter in the calculation, J_{0c} at each minicell would not be able to be extracted. Recently, two new methods to examine J_{0c} were reported by Saint-Cast *et al.* [9], [10]. One is an analytical model and the other is a Fourier analysis of PL images. Both methods are promising, we also compared these results with our data. A very good correlation was achieved. Griddler-AI [11], a finite-element method based numerical simulation software has

been used in several publications to extract J_{0c} parameters by a multivariate regression analysis of intensity-dependent photoluminescence (PL) images [12]–[16]. This approach significantly automates the extraction of J_{0c} and provides a rigorous and robust analysis routine to quantify the contact recombination losses. However, in the previous contributions, J_{0c} were treated as a global parameter and assumed to be uniform across the sample, even when minicells with different finger width and spacing were printed. Building onto previous work, a comprehensive analysis is performed in this work on J_{0c} at each of the minicells to get a better understanding of how J_{0c} changes with finger width and spacing.

In addition to recombination characteristics, the resistive characteristics also have a strong influence on cell performance. A common way to obtain contact resistivity (ρ_c) is by a transmission line method (TLM) [17], [18]. Due to its destructive nature, circular TLM (cTLM) is considered as a promising alternative [19]–[21]. Similar to characterization of J_{0c}, the impact of test structure design on the extracted ρ_c is rarely discussed, except in [21]. In this work, we present a comprehensive analysis of ρ_c with measurements performed on two different design of TLM structures, one with wide contact pad and one with narrow contact pad, as well as on cTLM.

Finally, to provide an explanation of the physical root cause of the variation on J_{0c} and ρ_c with varying finger width, spacing as well as firing temperature, scanning electron microscopy (SEM) imaging were performed to take cross-sectional and top-down SEM images at the metal–Si interface.

II. Experiment and Characterization

A. Test Structure Design

P-type 156 × 156 mm^2 pseudo-square Cz–Si wafers with a bulk resistivity of 2–5 Ω·cm were used in this study. After alkaline texturing, phosphorus diffusion was performed, resulting in an emitter sheet resistance (R_{emitter}) of 80±5 ohm/sq. After removing the PSG layer and the diffusion at the rear surface, antireflection coating of SiN$_x$ with a thickness of 78±4 nm is deposited on the front surface by plasma-enhanced chemical vapor deposition. The front sides were printed with Ag containing paste (DK92A, DK Electronic Materials, Inc.) and the rear sides were printed with full area Al paste (HY-1606, Jiangsu Hoyi Technology Company, Ltd.). As shown in Fig. 1, two different sets of test structures were printed on the front side of the samples. The main difference lies in the minicells, where in Fig. 1 (Left), the variation on the metal fraction was realized by changing the finger width from 60 μm to 80, 100, 120, 150, 250, and 400 μm, whereas the finger spacing was kept constant as 1.5 mm; in Fig. 1 (Right), the variation on the metal fraction was realized by changing the finger spacing from 0.3 mm to 0.8, 1, 1.2, 1.5, 2, and 2.5 mm, whereas the finger width was kept constant as 60 μm. For brevity, we will call the sample with variation on finger width, the *varying width*, and the sample with variation on finger spacing, the *varying spacing*. In the center of both *varying width* and *varying spacing* samples, two different designs of TLM, one with wide contact pad (the width of the pad was designed to be 2.5 mm) and one with
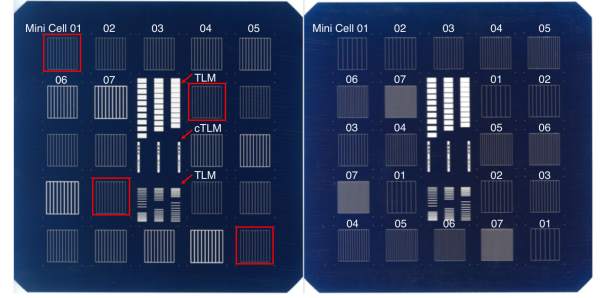

Fig. 1. Scanned images of the analyzed test structures. Minicells with varying metal contact fractions were printed with *varying width* and *varying spacing*. (Left) The *varying width* samples were designed to change finger width from 60 to 400 μm while spacing between the fingers was kept constant as 1.5 mm. (Right) The *varying spacings* were designed to change the finger spacing from 0.3 to 2.5 mm while the fingers were kept 60 μm. Two different designs of TLM structures of wide and narrow contact pads and cTLM structures were printed in the middle of the sample. The red boxes indicate examples of ROIs defined in Griddler-AI analysis.

narrow contact pad (the width of the pad was designed to be 0.3 mm), and cTLM structures were printed. For brevity, we will call the TLM structure with wide contact pad, the *wide*-TLM and the one with narrow contact pad, the *narrow*-TLM in the following discussions. After screen printing, both *varying width* and *varying spacing* samples were divided into five groups to receive firing at 740, 765, 790, 815, and 840 °C, which were the peak temperatures detected at the wafer surface using the DATAPAQ tool.

B. Intensity-Dependent Photoluminescence Imaging

A commercial PL tool (BT Imaging LIS-R1) was used in this work, featuring an 808-nm wavelength laser as the excitation source. Both *varying width* and *varying spacing* samples were imaged at four different illumination intensities ranging from 0.17 to 1.28 suns (1.28 suns is the highest illumination power can be achieved with the tool). The emitted PL signal was captured by a 1-megapixel silicon charge-coupled device camera equipped with a 920-nm long pass filter. Flat-field correction was applied to the captured PL images. A photon flux of 3.085 × 10^{17} cm^{-2}·s^{-1} is determined to be 1 sun by calibrating the photon flux toward matching the short-circuit current (J_{sc}) of a reference solar cell with known EQE data.

C. Griddler AI Analysis

The $J_{0c\text{-front}}$ values were extracted by analyzing the PL images with the autofitting routine built into Griddler-AI [11]. A detailed explanation of the autofitting routine in Griddler-AI can be found in [12]. Here, we just briefly explain. An Auto-CAD file representing the metal grid design of the sample can be imported into Griddler-AI. Two separate models for *varying width* and *varying spacing* samples were built. After importing the Auto-CAD file, Griddler-AI meshes the cell plane into about 1 × 10^5 triangular elements with more than 5 × 10^4 nodes and calculates the voltage distribution across the wafer plane at each of the nodes. As pointed out by Herrmann *et al.* [8],
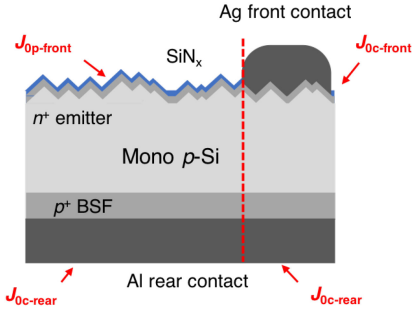
Fig. 2. Schematic illustration of cross-sectional view of the sample. In the analysis, $J_{0p\text{-front}}$ was assigned to the front side passivated region, $J_{0c\text{-front}}$ was assigned to the front side metallized region and $J_{0c\text{-rear}}$ was assigned to the rear surface.

Fig. 4. Extracted contact recombination $J_{0c\text{-front}}$ of the minicells with *varying spacing* as a function of metal fraction. Each data point represents an average of the minicells that have the same metal fraction and printed on one wafer. Different colors denote the five different groups of firing temperatures. The lines indicate a guide for the eye. The "+" symbols depict relevant results published in the literature.
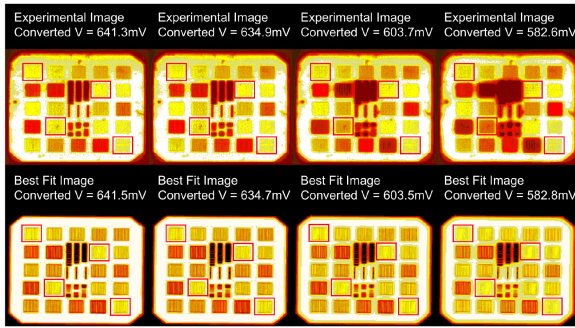

Fig. 3. Experimental (top row) and Griddler-AI simulated (bottom row) best fit PL images. The difference in voltages between the measured and fitted images is within 1 mV. The red boxes indicate the ROIs analyzed.

previous methods to extract the saturation current density at the metallized region often applies an area-weighted model, which assumes a uniform carrier distribution within the sample. This leads to an underestimation of the extracted saturation current density at the metallized region. However, this is not the case in Griddler-AI, since it calculates the voltage at each of the nodes and it is fully capable of simulating the balancing currents that occur in the cell plane under illumination conditions during imaging. Lateral carrier diffusion in the bulk is neglected, as highly doped emitters were formed in the samples used in this analysis. As has been explained in [12], Griddler-AI assigns different saturation current density values to the nodes located in the passivated region and the metallized region at the front surface and at the rear surface. Here, as shown in Fig. 2, $J_{0p\text{-front}}$ was assigned to the nodes that located at the front surface in the passivated region, $J_{0c\text{-front}}$ was assigned to the nodes that located at the front surface in the metallized region, and $J_{0c\text{-rear}}$ was assigned to the nodes that located at the rear surface. Instead of performing a pixel-by-pixel parameter extraction, different region-of-interest (ROI) can be defined within the wafer plane. Griddler-AI compares the calculated PL signal to the measured one within the defined ROI and automatically adjusts the various J_0 values defined for the different regions (passivated region and metallized region), until the converted voltage between the measurement and simulation is less than 1 mV, a "best fit" between the simulated and measured PL is achieved. Fig. 3 shows an example of the experimental and best fit PL images.
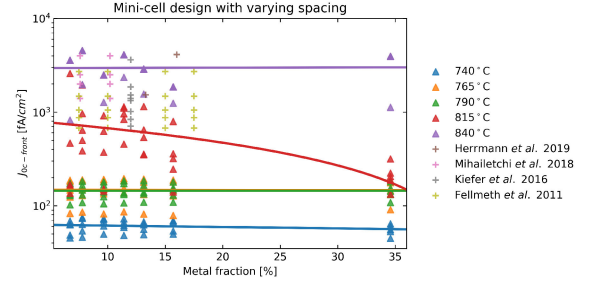
Here, the sample analyzed was *varying width* minicell 01. In the previous contribution [12], all the minicells were selected at the same time, representing the situation where $J_{0c\text{-front}}$ is assumed to be the same at different minicells. In this work, only the minicells with the same metal-fraction were selected at each time, as indicated in Figs. 1 and 3. This allows us to extract $J_{0c\text{-front}}$ for each of the minicells instead of assuming a global $J_{0c\text{-front}}$ for all the metallized region, and get a more detailed understanding of how the $J_{0c\text{-front}}$ changes with varying finger width and spacing.

D. Contact Resistivity Measurements

For contact resistivity measurements, *wide*-TLM and *narrow*-TLM structures were carefully laser scribed from the sample, whereas the *c*TLM structures were measured directly without cutting the structure out. A Brightspot ContactSpot measurement tool was used in the measurement of TLM structures, and a BrightSpot ContactSpot-PRO was used for *c*TLM measurements.

E. Scanning Electron Microscopy Imaging

Cross-sectional SEM images for *varying width* samples fired at 740 and 840 °C were obtained in secondary electron mode using a Zeiss ultra 55 SEM. To perform the top-down SEM imaging, the samples were treated by a similar approach reported by Ferrrada *et al.* [22]. Ag bulk was removed by dipping the sample in 70% nitric acid (HNO$_3$) for 90 min at 45 °C and the glass layer was removed by dipping the samples in 5% hydrofluoric (HF) for 4 min. in total (dipped 7–8 times, 30 s each) at room temperature.

III. RESULTS AND DISCUSSION

A. Influence of Minicell Design on Contact Recombination

Using Griddler-AI, the saturation current density at the front side Ag fingers ($J_{0c\text{-front}}$) was extracted from each of the minicells.

Fig. 4 shows the extracted $J_{0c\text{-front}}$ of the minicells with *varying spacing*. It is observed that $J_{0c\text{-front}}$ increases with
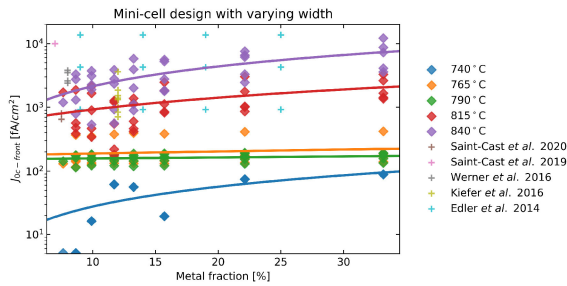
Fig. 5. Extracted contact recombination $J_{0c\text{-front}}$ of the minicells with varying finger width as a function of metal fraction. Each data point represents an average of the minicells that have the same metal fraction and printed on one wafer. Different colors denote the five different groups of firing temperatures. The lines indicate a guide for the eye. The "+" symbols depict relevant results published in the literature.

Fig. 6. V_{oc} determined by suns-V_{oc} method plotted as a function of metal fraction. The lines indicate a guide for the eye.

increasing firing temperature. $J_{0c\text{-front}}$ increases from ≈ 100 to ≈ 3000 fA/cm^2, when the firing temperature increases from 740 to 840 °C. It shows that $J_{0c\text{-front}}$ are almost constant with the increasing metal fraction. We see that for four groups of samples, $J_{0c\text{-front}}$ are almost straight lines when plotted with increasing metal fraction, except for samples fired at 815 °C, which shows a decreasing $J_{0c\text{-front}}$. The reason for the decreasing $J_{0c\text{-front}}$ of 815 °C sample is unclear. The constant $J_{0c\text{-front}}$ of *varying spacing* samples that were fired at the same temperature is expected, since $J_{0c\text{-front}}$ is an area-weighted parameter representing the recombination property at the metal–Si interface. Since the finger width was kept constant, the recombination property is expected to remain the same at the metal–Si interface.

Fig. 5 shows the extracted $J_{0c\text{-front}}$ of the minicells with *varying width*. Interestingly, it is observed that $J_{0c\text{-front}}$ increases significantly with increasing finger width, especially for the samples fired at a higher temperature. $J_{0c\text{-front}}$ increases from ≈ 2000 to ≈ 8100 fA/cm^2 for samples fired at 840 °C, when the metal fraction increases from 8% to 35%, which is realized by increasing the finger width from 60 to 400 μm. The results suggest that when the finger width is different, the recombination and resistive properties at the metal–Si interface changes. With a wider finger, more recombination is happening at the metal–Si interface. Meanwhile, a lower contact resistivity is observed, detailed results are presented in Section III-B. This trend of increasing $J_{0c\text{-front}}$ becomes less obvious when the firing temperature is lower. For example, $J_{0c\text{-front}}$ only increases from ≈ 1000 to ≈ 2100 fA/cm^2 for samples fired at 815 °C, but remains nearly constant at around ≈ 200 fA/cm^2 for samples fired at temperature lower than 790 °C. For samples fired at 740 °C, very low $J_{0c\text{-front}}$ of ≈ 100 fA/cm^2 was extracted, indicating nearly none recombination happening at the metal–Si interface. Correspondingly, an extremely high contact resistivity was observed on these samples. This is caused by under-firing the contact, where poor electrical contact is formed. We believe the trend we see is related to the microstructure formed during the firing process of the screen-printed contacts. It is known that glass frit is added to the screen-printing paste to help etch through the dielectric layer and make electrical contact to the doped layer in Si wafer. When printing a wider finger, more glass frit is printed to the surface. More thorough etching of
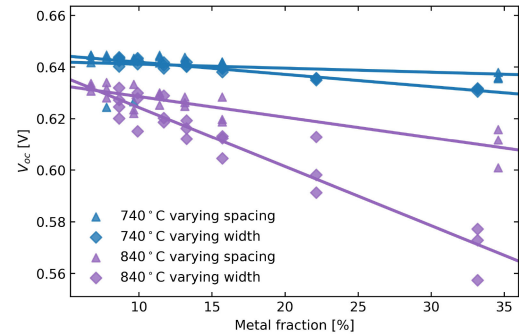
the dielectric layer could happen and more Ag crystallites could be formed at the metal–Si interface. This will help to form a better electrical contact; however, also provides a highly recombination active surface. In Section III-C, cross-sectional and top-down SEM images were presented to show the difference in the microstructures.

Additionally, contact recombination parameters extracted by several other approaches reported in the literature in the past decade [2], [3], [8]–[10], [23], [25] were also plotted in Figs. 4 and 5, indicated by the "+" symbols. It can be seen that $J_{0c\text{-front}}$ is consistent with what has been reported in the literature, especially for samples fired at 815 and 840 °C. This is because 815 and 840 °C represent optimum or slightly over-fire conditions for the paste studied in this work. Whereas 790, 765, and 740 °C represent the under-fire conditions, so that lower $J_{0c\text{-front}}$ was observed.

Furthermore, suns-V_{oc} measurements were performed to validate the extracted $J_{0c\text{-front}}$ results. Fig. 6 shows the probed V_{oc} results at each of the minicells of the *varying spacing* sample and *varying width* sample fired at 740 and 840 °C. The purpose of the suns-V_{oc} measurements is to provide a validation to the different $J_{0c\text{-front}}$ extracted from different minicells. The assumption is that if $J_{0c\text{-front}}$ is constant at different minicells, then due to increasing metal fraction, we would see a decreasing V_{oc}. However, if $J_{0c\text{-front}}$ is also increasing with increasing metal faction (only for the case with finger width, as discussed previously), then we would expect a steeper slop of decreasing V_{oc} as a function of metal fraction. Fig. 6 clearly shows that for 840 °C *varying width* sample, V_{oc} decreases much faster than the other groups. This confirms the observations from the extracted $J_{0c\text{-front}}$, where this group also showed the most dramatic increase.

B. Influence of TLM/cTLM Design on Contact Resistivity

Fig. 7 shows the measured contact resistivity (ρ_c) on cTLM, *wide*-TLM, and *narrow*-TLM of the samples fired at five different firing temperatures. First, as expected, ρ_c decreases with increasing firing temperature. We see ρ_c decreases from a mean value of 18.6 to 2.3 m$\Omega\cdot$cm^2 when the firing temperature increases from 740 to 815 °C. This matches with what we see in $J_{0c\text{-front}}$, which increases with firing temperature. It is observed that a higher ρ_c was measured on *narrow*-TLM than
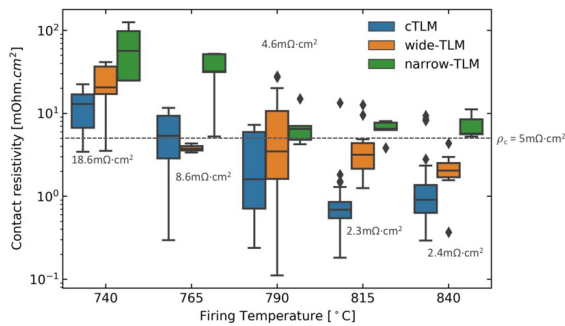
Fig. 7. Box plot shows contact resistivity (ρ_c) measured on *c*TLM, *wide*-TLM and *narrow*-TLM structures. The plot also shows contact resistivity of different firing temperature. For each firing temperature, a mean value for the three different structures is calculated. A line of $\rho_c = 5\text{m}\Omega \cdot \text{cm}^2$ separates the high and low contact resistivity region.
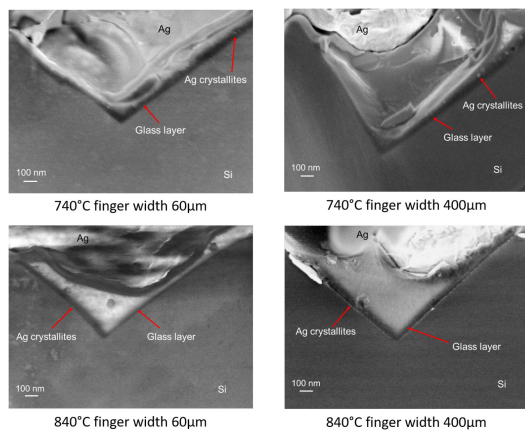

Fig. 8. Cross-sectional SEM images of samples with varying finger width. (Top-left) Minicell 01 (finger width 60 μm) of 740 °C; (Top-right) Minicell 07 (finger width 400 μm) of 740 °C; (Bottom-left) Minicell 01 of 840 °C; (Bottom-right) Minicell 07 of 840 °C.

on *wide*-TLM. For a firing temperature of 840 °C, a mean value of 1.7, 2.2, and 7.2 mΩ·cm^2 was measured on *c*TLM, *wide*-TLM, and *narrow*-TLM structures, respectively. This is also consistent with the $J_{\text{0c-front}}$ results reported in the previous section, where $J_{\text{0c-front}}$ was observed to be higher on minicells with wider fingers. We believe this relates to the difference in the microstructure formed at the metal–Si interface after the firing process. When a wider finger is printed, a higher amount of glass frit is contained in the paste, which could better assist the etching through the dielectric layer as well as the formation of more Ag crystallites at the metal–Si interface. Thus, a better electrical contact could be formed. In the next section, we show results of cross-sectional as well as top-down SEM images taken at the metal–Si interface of samples with different finger widths and fired at different temperatures to explain the difference in the microstructure. We believe this is the physical root cause behind the trend we see in the results of $J_{\text{0c-front}}$ and ρ_c.

C. Scanning Electron Microscopy Imaging of the Metal–Si Interface

Cross-sectional SEM imaging and top-down SEM imaging were performed to gain more insight into the microstructures
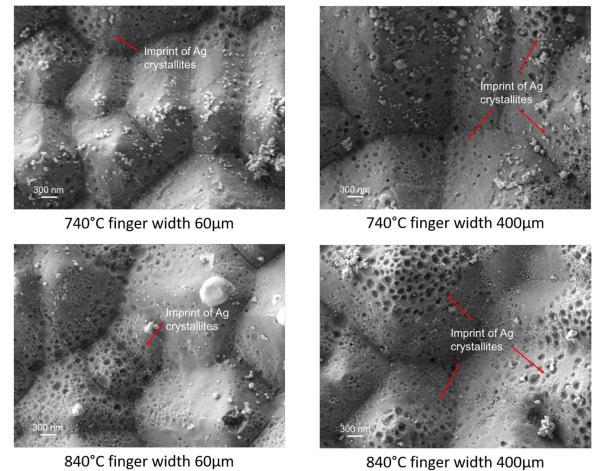

Fig. 9. Top-down SEM images of samples with varying finger width. (Top-left) Minicell 01 (finger width 60 μm) of 740 °C; (Top-right) Minicell 07 (finger width 400 μm) of 740 °C; (Bottom-left) Minicell 01 of 840 °C; (Bottom-right) Minicell 07 of 840 °C.

formed at the metal–Si interface. Fig. 8 shows the SEM images of samples fired at 740 and 840 °C. From left to right are SEM images took at the thinnest finger (minicell 01 in *varying width* sample), the widest finger (minicell 07 in *varying width* sample). It shows that the thicknesses of the glass layer in samples fired at 840 °C are significantly lower than that of the sample fired at 740 °C. Additionally, as the finger becomes wider, the glass layer becomes thinner as well. Also, we see not only the glass layer was thicker with 740 °C firing but also the Ag nanocrystals formed mostly located at the Ag side and not much penetrating into the glass layer. However, for the samples firing at 840 °C, most Ag nanocrystals went through the glass layer and some maybe in contact with Si, causing significant recombination, resulting in higher $J_{\text{0c-front}}$ and lower ρ_c. A thinner glass layer increases the tunneling propability for carriers, and therefore, the contact resistivity should decrease as more carriers are able to conduct through the interface. Meanwhile, thinner glass layer also facilitates carrier recombination. This is consistent with that in [24] and [25]. Fig. 9 shows the corresponding top-down SEM images of the samples. It is observed that the number of Ag crystallites formed in the samples fired at 840 °C was significantly higher. More Ag crystallites were observed in minicell 07 (finger width 400 μm) than minicell-01 (finger width 60 μm). Obviously, more Ag crystallites assist a better conduction of carriers. However, direct-contact of Ag with the Si emitter also provides a highly recombination active surface. These differences in the microstructure explains why higher $J_{\text{0c-front}}$ and lower ρ_c values are observed on samples fired at a higher temperature and at wider fingers.

IV. Conclusion

This work presents a comprehensive analysis of metallization-induced contact recombination losses and contact resistivity losses in screen-printed solar cells. In previous works, $J_{\text{0c-front}}$ is often assumed to be uniform across a wafer where minicells with varying finger width and/or varying spacing are printed. Our

This article has been accepted for inclusion in a future issue of this journal. Content is final as presented, with the exception of pagination.

6   IEEE JOURNAL OF PHOTOVOLTAICS

results show that $J_{0c\text{-front}}$ significantly increases with increasing finger width, whereas finger spacing has a negligible impact on $J_{0c\text{-front}}$. ρ_c is lower on a *wide*-TLM than a *narrow*-TLM structure. With further analysis of SEM imaging, we show higher temperature and wider finger result in thinner glass layer and more Ag crystallites formation, which explain the higher $J_{0c\text{-front}}$ and lower ρ_c values observed.

ACKNOWLEDGMENT

REFERENCES

[1] R. Hoenig *et al.*, "New measurement method for the investigation of space charge region recombination losses induced by the metallization of silicon solar cells," *Energy Procedia*, vol. 8, pp. 694–699, 2011, doi: 10.1016/j.egypro.2011.06.203.

[2] T. Fellmeth *et al.*, "Recombination at metal-emitter interfaces of front contact technologies for highly efficient silicon solar cells," *Energy Procedia*, vol. 8, pp. 115–121, 2011, doi: 10.1016/j.egypro.2011.06.111.

[3] A. Edler *et al.*, "Metallization-induced recombination losses of bifacial silicon solar cells," *Prog. Photovolt.: Res. Appl.*, vol. 23, no. 5, pp. 620–627, Feb. 2014, doi: 10.1002/pip.2479.

[4] D. Inns, "Understanding metal induced recombination losses in silicon solar cells with screen printed silver contacts," *Energy Procedia*, vol. 98, pp. 23–29, Nov. 2016, doi: 10.1016/j.egypro.2016.10.077.

[5] T. Aoyama, M. Aoki, I. Sumita, Y. Yoshino, and A. Ogura, "Effects of aluminum in metallization paste on the electrical losses in bifacial N-type crystalline silicon solar cells," *Energy Procedia*, vol. 98, pp. 106–114, Nov. 2016, doi: 10.1016/j.egypro.2016.10.086.

[6] L. J. Koduvelikulathu *et al.*, "Two-dimensional modeling of the metallization-induced recombination losses of screen-printed solar cells," *IEEE J. Photovolt.*, vol. 5, no. 1, pp. 159–165, Jan. 2015.

[7] F. Kiefer *et al.*, "Structural investigation of printed Ag/Al contacts on silicon and numerical modeling of their contact recombination," *IEEE J. Photovolt.*, vol. 6, no. 5, pp. 1175–1182, Sep. 2016.

[8] D. Herrmann *et al.*, "Numerical simulations of photoluminescence for the precise determination of emitter contact recombination parameters," *IEEE J. Photovolt.*, vol. 9, no. 6, pp. 1759–1767, Nov. 2019.

[9] P. Saint-Cast and A. Fell, "An analytical model for resistance-limited recombination at line defects in solar cells," *IEEE J. Photovolt.*, vol. 9, no. 5, pp. 1366–1373, Sep. 2019.

[10] P. Saint-Cast, D. Herrmann, and H. Hffler,"Information on recombination under front fingers based on Fourier analysis of photoluminescence images," *IEEE J. Photovolt.*, vol. 10, no. 2, pp. 554–559, Mar. 2020.

[11] J. Wong, J. W. Ho, D. Inns, and F. Fruhauf, "Luminescence image analysis using finite-element models: Finished solar cell analysis," *IEEE J. Photovolt.*, vol. 10, no. 1, pp. 159-165, Jan. 2020.

[12] M. Li, J. Wong, N. Chen, A. G. Aberle, and R. Stangl, "Determination of metallization-induced recombination losses of screen-printed silicon solar cell contacts and their dependence on the doping profile," *IEEE J. Photovolt.*, vol. 8, no. 6, pp. 1470–1477, Nov. 2018.

[13] V. Shanmugam, T. Mueller, A. G. Aberle, and J. Wong, "Determination of metal contact recombination parameters for silicon wafer solar cells by photoluminescence imaging," *Solar Energy*, vol. 118, pp. 20–27, 2015, doi: 10.1016/j.solener.2015.05.010.

[14] D. Ananthanarayanan *et al.*, "Determination of metal-induced recombination of n-type bifacial Si solar cells using special print patterns," *IEEE J. Photovolt.*, vol. 9, no. 3, pp. 643–651, May 2019.

[15] P. Padhamnath *et al.*, "Metal contact recombination in monoPoly solar cells with screen-printed & fire-through contacts," *Solar Energy Mater. Solar Cells*, vol. 192, pp. 109–116, 2019, doi: 10.1016/j.solmat.2018.12.026.

[16] M. Li, N. Iqbal, X. Lin, Z. Yang, and K. Davis, "Characterization of the metallization induced recombination losses in industrial silicon solar cells," in *Proc. IEEE 46th Photovolt. Specialists Conf.*, 2019, pp. 2769–2773.

[17] D. K. Schroder and D. L. Meier, "Solar cell contact resistance—A review," *IEEE Trans. Electron Devices*, vol. ED-31, no. 5, pp. 637–647, May 1984.

[18] S. Guo, G. Gregory, A. M. Gabor, W. V. Schoenfeld, and K. O. Davis, "Detailed investigation of TLM contact resistance measurements on crystalline silicon solar cells," *Solar Energy*, vol. 151, pp. 163–172, Jul. 2017, doi: 10.1016/j.solener.2017.05.015.

[19] G. Gregory *et al.*, "Non-destructive contact resistivity measurements on solar cells using the circular transmission line method," in *Proc. IEEE 44th Photovolt. Specialist Conf.*, 2017, pp. 74–78.

[20] S. Xiong *et al.*, "Application of CTLM method combining interfacial structure characterization to investigate contact formation of silver paste metallization on crystalline silicon solar cells," *Solid-State Electron.*, vol. 142, pp. 1–7, Apr. 2018, doi: 10.1016/j.sse.2017.12.012.

[21] G. Gregory *et al.*, "Nondestructive contact resistivity measurements on solar cells using the circular transmission line method," *IEEE J. Photovolt.*, vol. 9, no. 6, pp. 1800–1805, Nov. 2019.

[22] P. Ferrada *et al.*, "Interface analysis of Ag/n-type Si contacts in n-type PERT solar cells," *Prog. Photovolt.: Res. Appl.*, vol. 28, pp. 358–371, 2020, doi: 10.1002/pip.3242.

[23] S. Werner, E. Lohmuller, A. Wolf, and F. Clement, "Extending the limits of screen-printed metallization of phosphorus- and boron-doped surfaces," *Solar Energy Mater. Solar Cells*, vol. 158, pp. 37–42, 2016.

[24] M. M. Hilali *et al.*, "Effect of glass frit chemistry on the physical and electrical properties of thick-film Ag contacts for silicon solar cells," *J. Electron. Mater.*, vol. 35, no. 11, pp. 2041–2047, Nov. 2006, doi: 10.1007/s11664-006-0311-x.

[25] V. D. Mihailetchi, H. Chu, and R. Kopecek, "Insight into metal induced recombination losses and contact resistance in industrial silicon solar cells," in *Proc. IEEE 7th World Conf. Photovolt. Energy Convers. (Joint Conf. 45th IEEE PVSC 28th PVSEC & 34th EU PVSEC)*, 2018, pp. 2673–2677.